

# Scalable Graphene Coatings for Enhanced Condensation Heat Transfer

Daniel J. Preston,<sup>†</sup> Daniela L. Mafra,<sup>‡</sup> Nenad Miljkovic,<sup>†,§</sup> Jing Kong,<sup>‡</sup> and Evelyn N. Wang<sup>\*,†</sup>

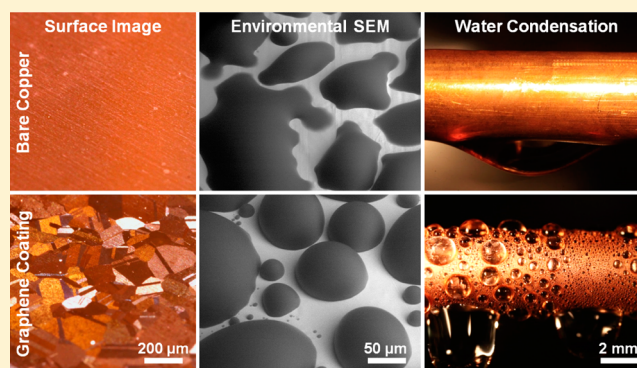
<sup>†</sup>Department of Mechanical Engineering and <sup>‡</sup>Department of Electrical Engineering and Computer Science, Massachusetts Institute of Technology, Cambridge, Massachusetts 02139, United States

<sup>§</sup>Department of Mechanical Science and Engineering, University of Illinois, Urbana, Illinois 61801, United States

## S Supporting Information

**ABSTRACT:** Water vapor condensation is commonly observed in nature and routinely used as an effective means of transferring heat with dropwise condensation on nonwetting surfaces exhibiting heat transfer improvement compared to filmwise condensation on wetting surfaces. However, state-of-the-art techniques to promote dropwise condensation rely on functional hydrophobic coatings that either have challenges with chemical stability or are so thick that any potential heat transfer improvement is negated due to the added thermal resistance of the coating. In this work, we show the effectiveness of ultrathin scalable chemical vapor deposited (CVD) graphene coatings to promote dropwise condensation while offering robust chemical stability and maintaining low thermal resistance. Heat transfer enhancements of 4× were demonstrated compared to filmwise condensation, and the robustness of these CVD coatings was superior to typical hydrophobic monolayer coatings. Our results indicate that graphene is a promising surface coating to promote dropwise condensation of water in industrial conditions with the potential for scalable application via CVD.

**KEYWORDS:** Graphene, condensation, dropwise, heat transfer enhancement, robust, scalable



Graphene is a two-dimensional material composed of carbon atoms arranged in a hexagonal lattice that has received significant attention since 2004 due to its unique and remarkable physical properties.<sup>1</sup> Prominent examples of the applicability of graphene include electronic device interconnects due to high charge carrier mobility,<sup>2</sup> transparent electrodes for solar cell devices,<sup>3</sup> and membranes for water desalination.<sup>4</sup> Graphene has also been used in thermal management applications due to its ability to improve device thermal conductivity and spread heat.<sup>5</sup> However, with graphene being a relatively new material, many applications have not yet been thoroughly explored.

One such application is the promotion of dropwise condensation. In typical industrial systems, condensed vapor forms a thin liquid film on the condenser surface due to the high surface energy associated with the majority of industrial heat exchanger materials (i.e., clean metals and metal oxides). This mode, known as filmwise condensation, is not desired due to the large thermal resistance to heat transfer.<sup>6</sup> Conversely, on low surface energy materials, the condensed vapor forms discrete liquid droplets. During this dropwise mode of condensation, droplets roll off at sizes approaching the capillary length (~2 mm for water) and clear the surface for renucleation, commonly resulting in 5–7× higher heat transfer performance compared to filmwise condensation.<sup>7</sup>

Dropwise condensation is typically achieved by functionalizing the condenser surface with a hydrophobic coating, for example, a fluorocarbon monolayer, wax, or polymer.<sup>7a,8</sup> Monolayer coatings (~1 nm thick) of long-chain fluorocarbons or fatty acids can induce hydrophobicity with negligible added thermal resistance but are often not robust, that is, chemically stable, over extended periods of time and therefore unsuitable in industrial applications.<sup>7a,9</sup> Thicker polymer coatings (>1 μm) such as PTFE have shown the potential to maintain robust hydrophobicity, but typically have a large thermal resistance that can negate the heat transfer enhancement gained by promoting dropwise condensation.<sup>7a</sup> More recently developed methods such as initiated chemical vapor deposition (iCVD) and plasma enhanced chemical vapor deposition (PECVD) have been used to grow ultrathin (<40 nm) conformal polymer coatings with success in achieving dropwise condensation.<sup>9b,10</sup> However, the durability of iCVD and PECVD coatings requires further characterization due to limited extended testing to assess mechanical wear and chemical stability for long-term condensing applications.

**Received:** December 2, 2014

**Revised:** March 22, 2015

**Published:** March 31, 2015

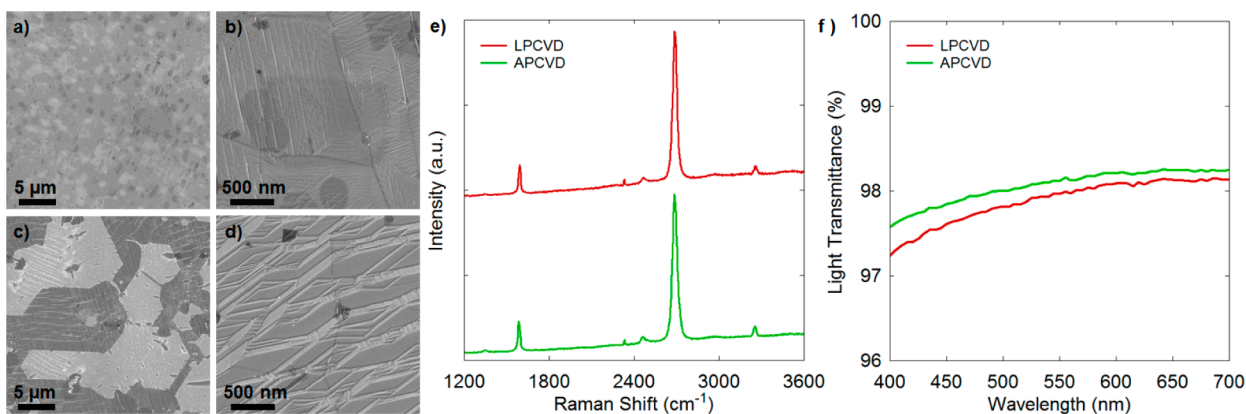


**Figure 1.** Field emission scanning electron microscopy images for (a,b) the low-pressure CVD graphene coating and (c,d) the atmospheric pressure CVD graphene coating on high-purity (>99.99%) copper substrates. During growth, the native copper oxide layer is reduced by H<sub>2</sub> gas at high temperature, and the underlying copper forms pronounced grains. Upon exposure to CH<sub>4</sub> at 1000 °C, graphene islands nucleate and grow over the surface until colliding with other islands. The copper grains remain visible. (e) Representative Raman spectra for the CVD graphene layers after transfer to a silicon substrate, obtained with a confocal Raman microscope using a 532 nm laser, demonstrate the presence of single-layer graphene for both CVD methods. (f) Optical characterization of the graphene transferred onto a transparent substrate indicated that both the LPCVD and APCVD graphene were predominately single-layer.<sup>22</sup>

Meanwhile, graphene displays hydrophobic behavior,<sup>11</sup> and its inert chemical nature and demonstrated mechanical strength suggest that it will resist degradation under typical condenser conditions.<sup>3,12</sup> Furthermore, the thermal resistance of a graphene coating is well-characterized<sup>13</sup> and is negligible in condensation applications (see Supporting Information, Section S2), and it can be applied relatively scalably via CVD.<sup>14</sup> Although graphene was initially suggested to have complete wetting transparency,<sup>15</sup> its hydrophobic nature has since been elucidated through careful experimental, numerical, and theoretical analysis.<sup>11,16</sup> Past work<sup>15</sup> also proposed graphene coatings to promote dropwise condensation, but the results of the experimental analysis did not show the expected improvement in heat transfer compared to filmwise condensation. The presence of noncondensable gases in the experimental setup not only reduced the improvement gained by promoting dropwise condensation to 30–40% as opposed to 500–700% but also resulted in reported condensation heat transfer coefficients 3 orders of magnitude lower than typical values without noncondensable gases.<sup>7a</sup> Furthermore, the mechanism for the dropwise condensation behavior was attributed to the “transparent” graphene layer protecting the copper from oxidation and preserving the intrinsic hydrophobic behavior of copper, while it has been demonstrated that copper is actually intrinsically hydrophilic<sup>17</sup> like other high-surface-energy materials.<sup>18</sup>

In this work, we demonstrated the uniform coating of high-purity (>99.99%) copper with graphene by both low and atmospheric pressure CVD. Both the low-pressure CVD (LPCVD) and the atmospheric pressure CVD (APCVD) graphene were single-layer. Subsequently, we experimentally demonstrated a 4× higher heat transfer coefficient for dropwise condensation of water on copper coated by graphene (both LPCVD and APCVD) compared to filmwise condensation on bare copper, which is in good agreement with theoretical models used for each case. The robustness of these graphene coatings was compared to a long-chain fluorocarbon monolayer commonly used to promote dropwise condensation, where 100 °C steam was condensed on both samples continuously. The fluorocarbon monolayer coating degraded completely in under 12 h, while for the graphene coatings, dropwise condensation

was observed over a two-week span without showing signs of degradation. These results suggest that graphene is a robust and nonreactive coating material that enhances condensation heat transfer by promoting dropwise condensation.

The copper samples used as substrates for graphene CVD were high purity tubes (>99.99%, OD = 1/4 in., McMaster-Carr) and sections of sheet metal (>99.99%, thickness = 0.032 in., McMaster-Carr). Prior to the CVD process, the copper samples were sonicated in acetone, triple-rinsed with deionized water, submersed in 2.0 M hydrochloric acid, again triple-rinsed with deionized water, and finally treated for 10 min with argon plasma (Harrick PDC-001), which removes hydrocarbons via physical bombardment.<sup>19</sup> This process was also used to clean the bare copper samples for characterization of filmwise condensation under ideal conditions because past work has shown that bare copper exhibits filmwise condensation during continuous condensation.<sup>20</sup>

The CVD processes were then performed on the copper samples at both low and atmospheric pressure in a 1 in. quartz tube furnace. For both processes, the furnace was heated to 1000 °C, and hydrogen gas (with a flow rate of 10 sccm) for the LPCVD process and argon gas (with a flow rate of 500 sccm) for the APCVD process flowed over the samples for 30 min prior to graphene growth. Methane gas was then introduced and the synthesis of graphene was performed over 30 min at 1.9 Torr and atmospheric pressure for the LPCVD (with a flow rate of H<sub>2</sub>/CH<sub>4</sub> = 70/4 sccm) and APCVD (with a flow rate of Ar/CH<sub>4</sub> = 500/3 sccm) coatings, respectively.<sup>21</sup> Finally, the samples were cooled to room temperature under hydrogen (10 sccm)/argon gas (500 sccm) for LPCVD/APCVD and then exposed to laboratory air (i.e., nonfiltered). While exposure to air leaves the possibility for contamination, the difference in wettability is expected to be negligible across different laboratory environments as indicated in past work<sup>18b</sup> (Further characterization specifically for graphene contamination under several different environments is an important topic and should be investigated in future research).

We characterized the samples using field-emission scanning electron microscopy (Zeiss Ultra-Plus) to determine the surface morphology, shown in Figure 1. Copper grains are visible on both the LPCVD and APCVD surfaces, and it was observed

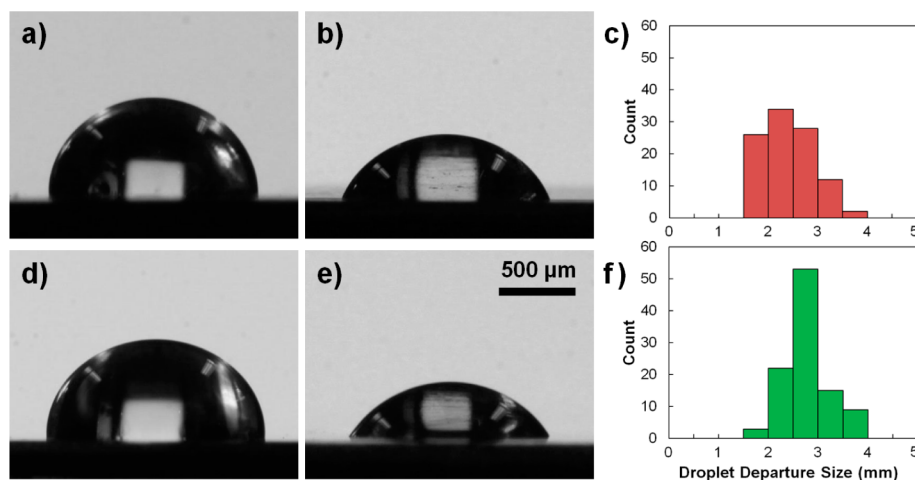


**Figure 2.** Representative images of (a) advancing and (b) receding contact angles of water on LPCVD graphene grown on a high-purity copper substrate, obtained by goniometric measurement. A histogram of droplet departure size during water condensation on LPCVD graphene is shown in (c). The advancing and receding contact angle for water on APCVD graphene are shown in (d) and (e), respectively, and a histogram of droplet departure size during water condensation on APCVD graphene is shown in (f). The average droplet departure diameter during water condensation on APCVD graphene is  $2.8 \pm 0.1$  mm compared to  $2.4 \pm 0.1$  mm on LPCVD graphene, suggesting a slightly higher expected condensation heat transfer coefficient on LPCVD graphene than on APCVD graphene.

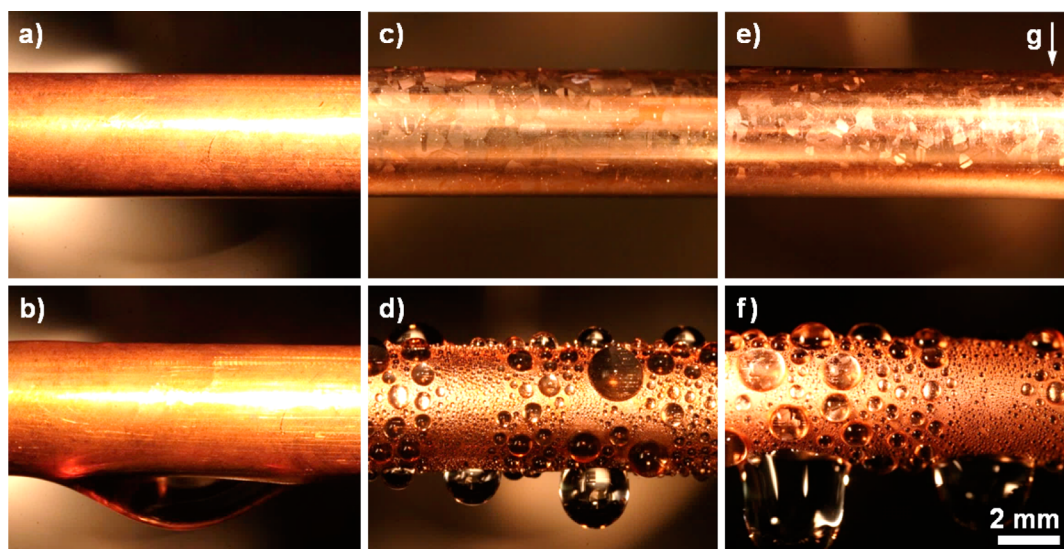


**Figure 3.** Photographs of a clean high-purity copper condenser tube (a) under vacuum and (b) undergoing filmwise condensation of deionized and degassed water vapor in the experimental vacuum chamber. Similarly, photographs of the graphene-coated high-purity copper condenser tubes are shown under vacuum and undergoing dropwise condensation of water with the LPCVD graphene coating in (c,d) and the APCVD graphene coating in (e,f).

that the graphene covered the entire surface of the copper. (The absence of visible copper grains on the bare copper surface is attributed to not heating the bare copper to  $1000\text{ }^{\circ}\text{C}$  as is required during graphene CVD.) Further characterization of the samples was conducted with Raman spectroscopy using a confocal Raman microscope with a 532 nm laser. Representative Raman spectra for the CVD graphene coatings after transfer onto a silicon substrate are shown in Figure 1e, where the ratio of 2D/G peaks ( $4\text{--}5\times$ ) and the full width at half-maximum of the 2D peak ( $25\text{--}30\text{ cm}^{-1}$ ) demonstrate the presence of single-layer graphene for both CVD methods. Optical characterization of the CVD graphene after transfer onto a transparent substrate (see Supporting Information) was also performed to study the graphene thickness over a larger area than the Raman laser spot size (Raman spot size is  $\sim 1\text{ }\mu\text{m}$

while the transmittance measurement spot size is  $\sim 5\text{ mm}$ ). The optical characterization indicated that both the LPCVD and APCVD graphene were predominately single-layer.<sup>22</sup>

We determined the surface wetting properties for water by goniometric characterization, where the advancing and receding contact angles in Figure 2 describe the surface wettability.<sup>23</sup> Both the advancing and receding contact angles need to be considered to determine the force that holds a droplet stationary on an inclined condensing surface against the force of gravity, which directly affects droplet departure size and condensation heat transfer.<sup>24</sup> The average advancing/receding contact angles were  $87 \pm 5^{\circ}/64 \pm 5^{\circ}$  for the LPCVD graphene and  $93 \pm 5^{\circ}/56 \pm 5^{\circ}$  for the APCVD graphene, determined from six points on each sample using a piezoelectric picoliter-scale droplet dispenser microgoniometer (Kyowa MCA-3) with

the receding contact angle obtained during droplet evaporation and observed to exhibit constant receding contact angle behavior.<sup>25</sup> The contact angle hysteresis was attributed to sporadic defects on the surface, possibly at graphene grain boundaries. The droplet departure size during water vapor condensation, defined as the diameter at which droplets begin to slide down the condenser wall, is shown in Figure 2c,f. The average droplet departure diameters were  $2.4 \pm 0.1$  mm on LPCVD graphene compared to  $2.8 \pm 0.1$  mm on APCVD graphene, suggesting that the condensation heat transfer coefficient on LPCVD graphene will be slightly higher than on APCVD graphene as droplets shed at smaller sizes and refresh the surface for renucleation. The contact angle on the clean bare copper surface was  $\sim 0^\circ$  with no distinction between advancing and receding.

We experimentally obtained the overall heat transfer performance of the graphene-coated copper tubes in a controlled vacuum chamber. Prior to condensation experiments, the vacuum chamber was evacuated to a pressure of  $P < 1.0$  Pa to eliminate the presence of noncondensable gases, which have been shown to severely degrade condensation heat transfer performance.<sup>26</sup> Water vapor was then introduced from a canister of degassed, deionized water attached to the vacuum chamber. The copper tube temperature was regulated by an internal chiller water flow loop which was isolated from the interior of the vacuum chamber, and the heat transfer through the tube wall was determined as a function of the chiller water flow rate and chiller water temperature at the tube inlet and outlet. As the copper tube was chilled internally, water vapor within the chamber condensed on the outer tube surface. The water vapor pressure within the chamber was maintained at values ranging from 2 to 5 kPa (corresponding to saturated water temperatures of 17 to 33 °C), which are typical for industrial condenser applications.<sup>27</sup>

Photographs of condensation on the exterior tube surfaces are shown in Figure 3. The bare copper tube underwent filmwise condensation of water vapor regardless of the temperature difference between the tube and the surrounding water vapor due to the spreading nature of water on clean copper (Figure 3a,b). The LPCVD (Figure 3c,d) and APCVD (Figure 3e,f) graphene coated tubes have visible graphene layers when dry (Figure 3c,e), and these coated tubes exhibited dropwise condensation over the full range of experimental conditions.

The overall heat flux, determined by the change in sensible heat of the chiller water, was obtained along with the log mean temperature difference (LMTD) between the chiller water and the temperature corresponding to the pressure of the surrounding water vapor for the bare copper (diamonds), LPCVD graphene (squares), and APCVD graphene (circles) (Figure 4a). The overall heat flux increased monotonically with the LMTD, where the local slope of this curve represents the overall heat transfer coefficient. Figure 4b shows the condensation heat transfer coefficient extracted from the overall heat transfer coefficient (see Supporting Information) as a function of vapor pressure while holding the supersaturation  $S = P_{\text{vapor}}/P_{\text{sat}}(T_{\text{wall}})$  constant ( $S = 1.2$ ). The theoretical predictions (dashed curves) were obtained from the droplet growth and distribution model for the graphene-coated condensers and from the Nusselt model for filmwise condensation on the bare copper condenser and were in good agreement with the experimental data (for model derivation and parameters, see Supporting Information). The assumption

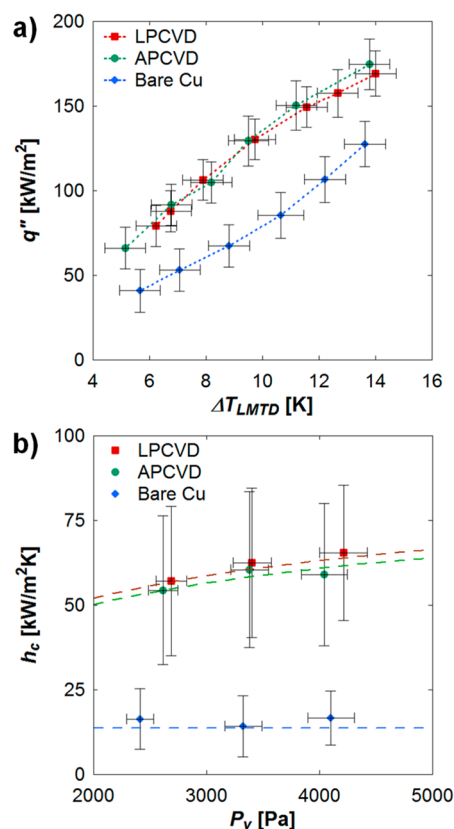


**Figure 4.** Water condensation heat transfer performance for the copper tubes with and without graphene coatings. The graphene-coated condensers exhibit dropwise condensation, while the bare copper undergoes filmwise condensation. Overall surface heat flux ( $q''$ ) is shown as a function of the steady state experimental chiller-water-to-vapor log mean temperature difference ( $\Delta T_{LMTD}$ ) in (a), where the slope of the data trend represents the overall heat transfer coefficient, that is, the combination of the chiller water flow, copper tube, graphene coating (for coated tubes), and condensation heat transfer coefficients. (b) Experimental (points) and theoretical (dashed curves) steady-state condensation heat transfer coefficient ( $h_c$ ), which includes graphene coatings where applicable, shown as a function of surrounding saturated vapor pressure ( $P_v$ ). Error bars indicate the propagation of error associated with the fluid inlet and outlet temperature differential ( $\pm 0.05$  K) and pressure measurement ( $\pm 2.5\%$ ). Theoretical predictions were obtained from the droplet growth and distribution model for the graphene-coated condensers with droplet departure size as an input parameter (for model derivation and parameters, see Supporting Information) and from the Nusselt model for filmwise condensation on the bare copper condenser.

of uniform wall temperature for the models was justified because the temperature variation in the chiller water from the inlet to outlet of the sample was over an order of magnitude less than the temperature difference from the sample to the surrounding vapor. The condensation heat transfer coefficient for the LPCVD and APCVD graphene coated copper tubes ( $\sim 60 \pm 20$  kW/m<sup>2</sup>K) was 4× greater than that measured for filmwise condensation on bare copper ( $\sim 15 \pm 9$  kW/m<sup>2</sup>K). Note that the dropwise condensation heat transfer coefficient decreases at low subcooling because the interfacial heat transfer coefficient becomes a major resistance to heat transfer,<sup>7a,8e,28</sup> while the filmwise condensation heat transfer coefficient increases at low subcooling as the film becomes thinner,<sup>6</sup> consequently, while a 4× enhancement was expected for the

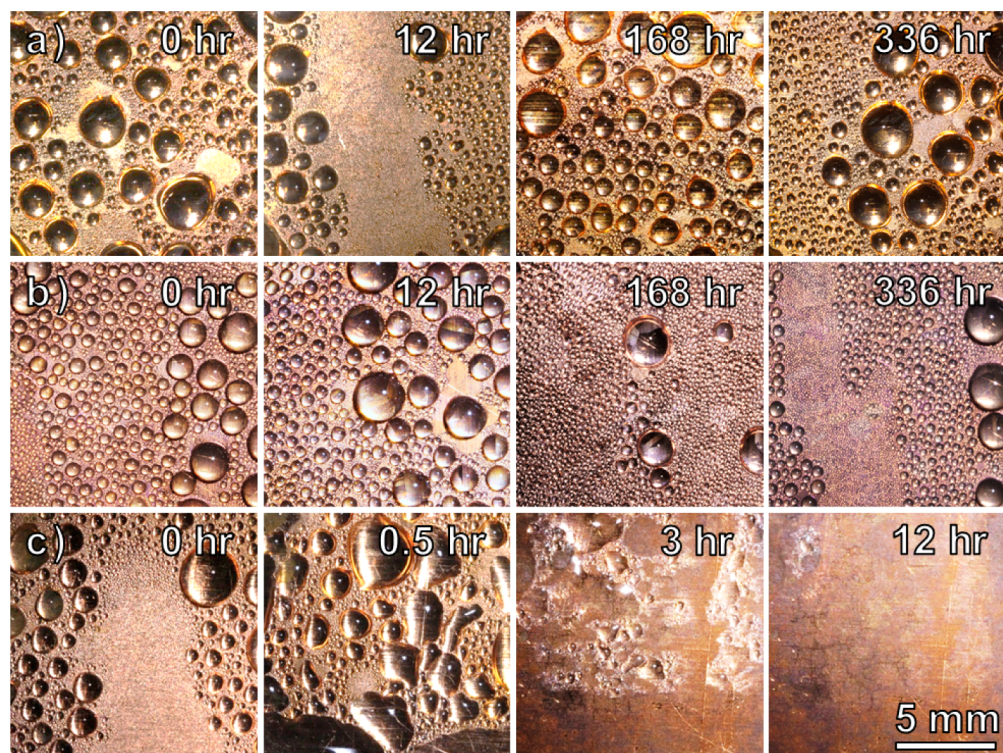


**Figure 5.** Time-lapse images of continuous condensation of 100 °C steam on (a) LPCVD, (b) APCVD, and (c) TFTS coatings on high-purity copper samples. The robust promotion of dropwise condensation by the graphene coatings is investigated over 2 weeks without showing signs of degradation, in contrast with the TFTS coating, which degraded and transitioned to filmwise condensation in less than 12 h.

subcooling range used to characterize the heat transfer coefficient in the present work (3.5–5 K), the typically reported 5–7 $\times$  heat transfer coefficient enhancement<sup>7a</sup> would be realized at higher subcooling (over  $\sim$ 10 K, see Supporting Information, Section S9).

The error for the condensation heat transfer coefficient was determined by propagating uncertainties associated with the chiller water thermocouples and mass flow meter, the pressure sensor inside the chamber, the sample surface area, and the Gnielinski correlation for heat transfer from the chiller water bulk to the internal surface of the sample. Since the condensation heat transfer coefficient,  $h_c$  is not simply a function of a product of powers, the error must be determined from the first partial derivatives of  $h_c$  with respect to its components along with the uncertainties of its components (described in detail in the Supporting Information, Section S5).

In addition to improved condensation heat transfer by promoting dropwise condensation, graphene coatings also exhibit inert chemical behavior and excellent mechanical strength, which are expected to result in improved resistance to routine wear during condensation and provide a robust alternative to current state-of-the-art dropwise functionalization coatings. For direct comparison, a monolayer coating of trichloro(1H,1H,2H,2H-perfluorooctyl)silane (TFTS) was applied to a clean copper sample and, along with the graphene-coated samples, underwent an accelerated endurance test that consisted of continuous condensation of 100 °C steam. The TFTS coating was applied via vapor-phase deposition, where the copper substrate was cleaned as described for the graphene CVD, but oxygen plasma was substituted for argon plasma. The copper substrate was then placed in a desiccator immediately following the oxygen plasma treatment along with a vial containing 2 mL of TFTS. The desiccator was evacuated with a

vacuum pump for 90 s, after which the sample was left in the TFTS vapor for 10 min. The sample was then removed from the desiccator, solvent rinsed, and dried with a clean nitrogen stream. The advancing/receding contact angles were  $120 \pm 5^\circ / 82 \pm 5^\circ$  on the TFTS-coated copper sample as fabricated.

The endurance test was performed in a controlled positive-pressure continuous condensation chamber (see Supporting Information, section S7). The samples were cooled to a surface temperature of  $95 \pm 1$  °C and exposed to a continuous supply of 100 °C steam provided from a reservoir of degassed, deionized water. Initially, dropwise condensation was observed on both the LPCVD and APCVD graphene coated samples and the TFTS-coated sample (first column of Figure 5). However, the TFTS coating degraded noticeably within the first 30 min of testing with decreased advancing and receding contact angles observed, and completely transitioned to filmwise condensation within 12 h (Figure 5c), likely due to stripping of the coating by oxidation (X-ray photoelectron spectroscopy (K-Alpha) revealed that only 3% of the originally observed atomic percent of fluorine, a primary component of TFTS, remained on the surface after the continuous condensation experiment).<sup>9c,29</sup> Conversely, the LPCVD- and APCVD-graphene coated samples both sustained dropwise condensation for over 2 weeks with no signs of degradation when the experiments were discontinued (Figure 5a,b). Additionally, these graphene coatings can be altered to multilayer graphene or even single-/multilayer graphene composites<sup>30</sup> without drastic effect on the heat transfer (because the added thermal resistance is negligible, see Supporting Information Section S2) and can thus potentially be tailored to better prevent oxidation if it poses a problem. Further discussion on graphene's chemical robustness is presented in the Supporting Information, Section S8.

While graphene offers a robust coating material to promote dropwise condensation on industrial metals, it is not a likely candidate to induce superhydrophobic behavior on micro- and nanostructured materials due to its relatively low advancing and receding contact angles compared to fluoropolymer coatings typically used for this application. While this eliminates the ability of graphene-coated surfaces to promote jumping droplet condensation,<sup>31</sup> the improvement in heat transfer coefficient of 4× provided by dropwise-promoting graphene coatings compared to filmwise condensation outweighs the marginal additional increase of 30–40% gained by jumping droplet condensation compared to dropwise condensation. Another potential limitation of these graphene coatings is their inability to induce dropwise condensation in systems that use low-surface-tension working fluids such as pentane; these fluids are expected to exhibit low contact angles and spread on graphene-coated surfaces, resulting in filmwise condensation.

This study demonstrates that graphene CVD coatings are a viable method to promote dropwise condensation of water in industrial conditions with a demonstrated improvement in heat transfer performance of 4× compared to clean industrial metals and superior robustness compared to state-of-the-art dropwise-promoting monolayer coatings as demonstrated under continuous condensation of 100 °C steam. This result promises significant energy savings in applications such as water harvesting, thermal management, industrial power generation, and building heating and cooling.

## ■ ASSOCIATED CONTENT

### Supporting Information

ESEM characterization of the CVD graphene coatings, coating thermal resistance scaling, operation of the controlled condensation chamber for heat transfer measurement, calculation of condensation heat transfer coefficient and error analysis, modeling of condensation heat transfer coefficient, and operation of the robustness characterization setup. This material is available free of charge via the Internet at <http://pubs.acs.org>.

## ■ AUTHOR INFORMATION

### Corresponding Author

\*E-mail: [enwang@mit.edu](mailto:enwang@mit.edu).

### Author Contributions

E.N.W., J.K., D.J.P., and N.M. conceived the initial idea of this research. E.N.W. and J.K. guided the work. D.L.M. and D.J.P. fabricated, functionalized, and characterized the experimental samples. D.J.P. carried out the experiments and collected and analyzed the data. D.J.P. and N.M. carried out the theoretical analysis. All authors were responsible for writing the paper and have given approval to the final version of the manuscript.

### Notes

The authors declare no competing financial interest.

## ■ ACKNOWLEDGMENTS

We gratefully acknowledge funding support from the Office of Naval Research (ONR) with Dr. Mark Spector as program manager. We also acknowledge the support from the National Science Foundation through the Major Research Instrumentation Grant for Rapid Response Research (MRI-RAPID) for the microgoniometer. D.J.P. acknowledges funding received by the National Science Foundation Graduate Research Fellowship under Grant 1122374. Any opinion, findings, conclusions, or

recommendations expressed in this material are those of the author(s) and do not necessarily reflect the views of the National Science Foundation. D.L.M. acknowledges the Brazilian agency CNPq. J.K. acknowledges the support through the STC Center for Integrated Quantum Materials from NSF (U.S.) Grant DMR-1231319. This work was performed in part at the Center for Nanoscale Systems (CNS), a member of the National Nanotechnology Infrastructure Network (NNIN), which is supported by the National Science Foundation under NSF Award No. ECS-0335765. CNS is part of Harvard University.

## ■ ABBREVIATIONS

CVD, chemical vapor deposition; APCVD, atmospheric pressure CVD; LPCVD, low pressure CVD; FESEM, field emission scanning electron microscope; ESEM, environmental scanning electron microscope

## ■ REFERENCES

- (1) (a) Novoselov, K. S.; Jiang, D.; Schedin, F.; Booth, T. J.; Khotkevich, V. V.; Morozov, S. V.; Geim, A. K. Two-dimensional atomic crystals. *Proc. Natl. Acad. Sci. U.S.A.* **2005**, *102* (30), 10451–10453. (b) Novoselov, K. S.; Geim, A. K.; Morozov, S. V.; Jiang, D.; Zhang, Y.; Dubonos, S. V.; Grigorieva, I. V.; Firsov, A. A. Electric field effect in atomically thin carbon films. *Science* **2004**, *306* (5696), 666–669.
- (2) Chen, X. Y.; Akinwande, D.; Lee, K. J.; Close, G. F.; Yasuda, S.; Paul, B. C.; Fujita, S.; Kong, J.; Wong, H. S. P. Fully Integrated Graphene and Carbon Nanotube Interconnects for Gigahertz High-Speed CMOS Electronics. *IEEE Trans. Electron Dev.* **2010**, *57* (11), 3137–3143.
- (3) (a) Li, X. S.; Zhu, Y. W.; Cai, W. W.; Borysiak, M.; Han, B. Y.; Chen, D.; Piner, R. D.; Colombo, L.; Ruoff, R. S. Transfer of Large-Area Graphene Films for High-Performance Transparent Conductive Electrodes. *Nano Lett.* **2009**, *9* (12), 4359–4363. (b) Wang, X.; Zhi, L. J.; Mullen, K. Transparent, Conductive Graphene Electrodes for Dye-Sensitized Solar Cells. *Nano Lett.* **2008**, *8* (1), 323–327.
- (4) (a) Humplik, T.; Lee, J.; O'Hern, S. C.; Fellman, B. A.; Baig, M. A.; Hassan, S. F.; Atieh, M. A.; Rahman, F.; Laoui, T.; Karnik, R.; Wang, E. N. Nanostructured materials for water desalination. *Nanotechnology* **2011**, *22*, 292001. (b) O'Hern, S. C.; Stewart, C. A.; Boutilier, M. S. H.; Idrobo, J. C.; Bhaviripudi, S.; Das, S. K.; Kong, J.; Laoui, T.; Atieh, M.; Karnik, R. Selective Molecular Transport through Intrinsic Defects in a Single Layer of CVD Graphene. *ACS Nano* **2012**, *6* (11), 10130–10138.
- (5) (a) Goli, P.; Ning, H.; Li, X. S.; Lu, C. Y.; Novoselov, K. S.; Balandin, A. A. Thermal Properties of Graphene-Copper-Graphene Heterogeneous Films. *Nano Lett.* **2014**, *14* (3), 1497–1503. (b) Malekpour, H.; Chang, K. H.; Chen, J. C.; Lu, C. Y.; Nika, D. L.; Novoselov, K. S.; Balandin, A. A. Thermal Conductivity of Graphene Laminate. *Nano Lett.* **2014**, *14* (9), 5155–5161. (c) Yan, Z.; Liu, G. X.; Khan, J. M.; Balandin, A. A. Graphene quilts for thermal management of high-power GaN transistors. *Nat. Commun.* **2012**, *3*, 827.
- (6) Nusselt, W. The surface condensation of water vapour. *Z. Ver. Dtsch. Ing.* **1916**, *60*, 541–546.
- (7) (a) Rose, J. W. Dropwise condensation theory and experiment: a review. *J. Power Energy* **2002**, *216* (A2), 115–128. (b) Schmidt, E.; Schurig, W.; Sellschopp, W. Condensation of water vapour in film- and drop form. *Z. Ver. Dtsch. Ing.* **1930**, *74*, 544–544.
- (8) (a) Das, A. K.; Kilty, H. P.; Marto, P. J.; Andeen, G. B.; Kumar, A. The use of an organic self-assembled monolayer coating to promote dropwise condensation of steam on horizontal tubes. *J. Heat Transfer* **2000**, *122* (2), 278–286. (b) Marto, P. J.; Looney, D. J.; Rose, J. W.; Wanniarachchi, A. S. Evaluation of Organic Coatings for the Promotion of Dropwise Condensation of Steam. *Int. J. Heat Mass Transfer* **1986**, *29* (8), 1109–1117. (c) Vemuri, S.; Kim, K. J. An

experimental and theoretical study on the concept of dropwise condensation. *Int. J. Heat Mass Transfer* **2006**, *49* (3–4), 649–657. (d) Vemuri, S.; Kim, K. J.; Wood, B. D.; Govindaraju, S.; Bell, T. W. Long term testing for dropwise condensation using self-assembled monolayer coatings of n-octadecyl mercaptan. *Appl. Therm Eng.* **2006**, *26* (4), 421–429. (e) Enright, R.; Miljkovic, N.; Alvarado, J. L.; Kim, K. J.; Rose, J. W. Dropwise Condensation on Micro- and Nano-structured Surfaces. *Nanoscale Microscale Thermophy. Eng.* **2014**, *18* (3), 223–250.

(9) (a) Boinovich, L. B.; Emelyanenko, A. M. Hydrophobic materials and coatings: Principles of design, properties and applications. *Usp. Khim.* **2008**, *77* (7), 619–638. (b) Paxson, A. T.; Yague, J. L.; Gleason, K. K.; Varanasi, K. K. Stable Dropwise Condensation for Enhancing Heat Transfer via the Initiated Chemical Vapor Deposition (iCVD) of Grafted Polymer Films. *Adv. Mater.* **2013**, *26* (3), 418–423. (c) Holden, K. M.; Wanniarachchi, A. S.; Marto, P. J.; Boone, D. H.; Rose, J. W. The Use of Organic Coatings to Promote Dropwise Condensation of Steam. *J. Heat Transfer* **1987**, *109* (3), 768–774.

(10) Miljkovic, N.; Preston, D. J.; Enright, R.; Wang, E. N. Electrostatic charging of jumping droplets. *Nat. Commun.* **2013**, *4*, 2517.

(11) (a) Raj, R.; Maroo, S. C.; Wang, E. N. Wettability of Graphene. *Nano Lett.* **2013**, *13* (4), 1509–1515. (b) Shin, Y. J.; Wang, Y. Y.; Huang, H.; Kalon, G.; Wee, A. T. S.; Shen, Z. X.; Bhatia, C. S.; Yang, H. Surface-Energy Engineering of Graphene. *Langmuir* **2010**, *26* (6), 3798–3802.

(12) (a) Li, X. L.; Zhang, G. Y.; Bai, X. D.; Sun, X. M.; Wang, X. R.; Wang, E.; Dai, H. J. Highly conducting graphene sheets and Langmuir-Blodgett films. *Nat. Nanotechnol.* **2008**, *3* (9), 538–542. (b) Blake, P.; Brimicombe, P. D.; Nair, R. R.; Booth, T. J.; Jiang, D.; Schedin, F.; Ponomarenko, L. A.; Morozov, S. V.; Gleason, H. F.; Hill, E. W.; Geim, A. K.; Novoselov, K. S. Graphene-Based Liquid Crystal Device. *Nano Lett.* **2008**, *8* (6), 1704–1708.

(13) (a) Balandin, A. A. Thermal properties of graphene and nanostructured carbon materials. *Nat. Mater.* **2011**, *10* (8), 569–581. (b) Seol, J. H.; Jo, I.; Moore, A. L.; Lindsay, L.; Aitken, Z. H.; Pettes, M. T.; Li, X. S.; Yao, Z.; Huang, R.; Broido, D.; Mingo, N.; Ruoff, R. S.; Shi, L. Two-Dimensional Phonon Transport in Supported Graphene. *Science* **2010**, *328* (5975), 213–216. (c) Renteria, J. D.; Nika, D. L.; Balandin, A. A. Graphene Thermal Properties: Applications in Thermal Management and Energy Storage. *Appl. Sci.* **2014**, *4* (4), 525–547.

(14) (a) Hesjedal, T. Continuous roll-to-roll growth of graphene films by chemical vapor deposition. *Appl. Phys. Lett.* **2011**, *98*, 133106. (b) Bae, S.; Kim, H.; Lee, Y.; Xu, X. F.; Park, J. S.; Zheng, Y.; Balakrishnan, J.; Lei, T.; Kim, H. R.; Song, Y. I.; Kim, Y. J.; Kim, K. S.; Ozyilmaz, B.; Ahn, J. H.; Hong, B. H.; Iijima, S. Roll-to-roll production of 30-in. graphene films for transparent electrodes. *Nat. Nanotechnol.* **2010**, *5* (8), 574–578.

(15) Rafiee, J.; Mi, X.; Gullapalli, H.; Thomas, A. V.; Yavari, F.; Shi, Y. F.; Ajayan, P. M.; Koratkar, N. A. Wetting transparency of graphene. *Nat. Mater.* **2012**, *11* (3), 217–222.

(16) (a) Shih, C. J.; Wang, Q. H.; Lin, S. C.; Park, K. C.; Jin, Z.; Strano, M. S.; Blankschtein, D. Breakdown in the Wetting Transparency of Graphene. *Phys. Rev. Lett.* **2012**, *109*, 176101. (b) Shih, C. J.; Strano, M. S.; Blankschtein, D. Wetting translucency of graphene. *Nat. Mater.* **2013**, *12* (10), 866–869.

(17) (a) Schrader, M. E. Ultrahigh-Vacuum Techniques in Measurement of Contact Angles 0.3. Water on Copper and Silver. *J. Phys. Chem.* **1974**, *78* (1), 87–89. (b) Trevo, D. J.; Johnson, H. The Water Wettability of Metal Surfaces. *J. Phys. Chem.* **1958**, *62* (7), 833–837.

(18) (a) Bewig, K. W.; Zisman, W. A. Wetting of Gold and Platinum by Water. *J. Phys. Chem.* **1965**, *69* (12), 4238–4242. (b) Preston, D. J.; Miljkovic, N.; Sack, J.; Enright, R.; Queeney, J.; Wang, E. N. Effect of hydrocarbon adsorption on the wettability of rare earth oxide ceramics. *Appl. Phys. Lett.* **2014**, *105*, 11601. (c) Schrader, M. E. Wettability of Clean Metal-Surfaces. *J. Colloid Interface Sci.* **1984**, *100* (2), 372–380. (d) Schrader, M. E. Ultrahigh-Vacuum Techniques in Measurement of

Contact Angles 0.2. Water on Gold. *J. Phys. Chem.* **1970**, *74* (11), 2313–2317. (e) Bernett, M. K.; Zisman, W. A. Confirmation of Spontaneous Spreading by Water on Pure Gold. *J. Phys. Chem.* **1970**, *74* (11), 2309–2312.

(19) (a) Umezu, I.; Kohno, K.; Aoki, K.; Kohama, Y.; Sugimura, A.; Inada, M. Effects of argon and hydrogen plasmas on the surface of silicon. *Vacuum* **2002**, *66* (3–4), 453–456. (b) Nickerson, R. Plasma surface modification for cleaning and adhesion. *Polymers, Laminations & Coatings Conference*, 1998; Tappi Press: Billerica, MA, Books 1 and 2; 1998; pp 1101–1108. (c) Wasy, A.; Balakrishnan, G.; Lee, S. H.; Kim, J. K.; Kim, D. G.; Kim, T. G.; Song, J. I. Argon plasma treatment on metal substrates and effects on diamond-like carbon (DLC) coating properties. *Cryst. Res. Technol.* **2014**, *49* (1), 55–62.

(20) (a) Erb, R. A. Wettability of Metals under Continuous Condensing Conditions. *J. Phys. Chem.* **1965**, *69* (4), 1306–1309. (b) Wilkins, D. G.; Bromley, L. A.; Read, S. M. Dropwise and Filmwise Condensation of Water Vapor on Gold. *AIChE J.* **1973**, *19* (1), 119–123. (c) Woodruff, D. W.; Westwater, J. W. Steam Condensation on Electroplated Gold - Effect of Plating Thickness. *Int. J. Heat Mass Transfer* **1979**, *22* (4), 629–632.

(21) (a) Bhaviripudi, S.; Jia, X. T.; Dresselhaus, M. S.; Kong, J. Role of Kinetic Factors in Chemical Vapor Deposition Synthesis of Uniform Large Area Graphene Using Copper Catalyst. *Nano Lett.* **2010**, *10* (10), 4128–4133. (b) Li, X. S.; Cai, W. W.; An, J. H.; Kim, S.; Nah, J.; Yang, D. X.; Piner, R.; Velamakanni, A.; Jung, I.; Tutuc, E.; Banerjee, S. K.; Colombo, L.; Ruoff, R. S. Large-Area Synthesis of High-Quality and Uniform Graphene Films on Copper Foils. *Science* **2009**, *324* (5932), 1312–1314. (c) Reina, A.; Jia, X. T.; Ho, J.; Nezich, D.; Son, H. B.; Bulovic, V.; Dresselhaus, M. S.; Kong, J. Large Area, Few-Layer Graphene Films on Arbitrary Substrates by Chemical Vapor Deposition. *Nano Lett.* **2009**, *9* (1), 30–35.

(22) Nair, R. R.; Blake, P.; Grigorenko, A. N.; Novoselov, K. S.; Booth, T. J.; Stauber, T.; Peres, N. M. R.; Geim, A. K. Fine structure constant defines visual transparency of graphene. *Science* **2008**, *320* (5881), 1308–1308.

(23) (a) Gao, L. C.; McCarthy, T. J. Wetting 101 Degrees. *Langmuir* **2009**, *25* (24), 14105–14115. (b) Gao, L. C.; McCarthy, T. J. Contact Angle Hysteresis Explained. *Langmuir* **2006**, *22* (14), 6234–6237.

(24) (a) Miljkovic, N.; Enright, R.; Wang, E. N. Modeling and Optimization of Superhydrophobic Condensation. *J. Heat Transfer* **2013**, *135* (11), 111004–111004. (b) Kim, S.; Kim, K. J. Dropwise Condensation Modeling Suitable for Superhydrophobic Surfaces. *J. Heat Transfer* **2011**, *133* (8), 081502–1–081502–7. (c) Rose, J. W.; Glicksman, L. R. Dropwise condensation - the distribution of drop sizes. *Int. J. Heat Mass Transfer* **1973**, *16*, 411–425. (d) Rumaa, J. Drop Size Distribution and Heat-Flux of Dropwise Condensation. *Chem. Eng. J.* **1978**, *16* (3), 171–176.

(25) Lam, C. N. C.; Wu, R.; Li, D.; Hair, M. L.; Neumann, A. W. Study of the advancing and receding contact angles: liquid sorption as a cause of contact angle hysteresis. *Adv. Colloid Interface Sci.* **2002**, *96* (1–3), 169–191.

(26) (a) Tanner, D. W.; Pope, D.; Potter, C. J.; West, D. Heat Transfer in Dropwise Condensation at Low Steam Pressures in Absence and Presence of Non-Condensable Gas. *Int. J. Heat Mass Transfer* **1968**, *11* (2), 181–182. (b) Sundaraman, T. G.; Venkatram, T. Heat-Transfer during Dropwise Condensation of Steam in Presence of Non-Condensable Gases - Effects of Geometrical Shape of Surface Reversal of Cooling Water-Flow and Orientation. *Indian J. Technol.* **1976**, *14* (7), 313–321.

(27) (a) Vosough, A.; Falahat, A.; Vosough, S.; Esfehiani, H. n.; Behjat, A.; Rad, R. n. Improvement Power Plant Efficiency with Condenser Pressure. *Int. J. Multidiscip. Sci. Eng.* **2011**, *2* (3), 38–43. (b) Bejan, A. Fundamentals of exergy analysis, entropy generation minimization, and the generation of flow architecture. *Int. J. Energy Res.* **2002**, *26* (7), 545–565.

(28) Wilmschurst, R.; Rose, J. W. *Dropwise Condensation—Further Heat Transfer Measurements*. In Fourth International Heat Transfer Conference; Elsevier: Paris-Versailles, 1970; Vol. 6.

(29) Leidheiser, H. Corrosion of Painted Metals - a Review. *Corrosion* **1982**, *38* (7), 374–383.

(30) Shahil, K. M. F.; Balandin, A. A. Graphene-Multilayer Graphene Nanocomposites as Highly Efficient Thermal Interface Materials. *Nano Lett.* **2012**, *12* (2), 861–867.

(31) (a) Boreyko, J. B.; Chen, C. H. Vapor chambers with jumping-drop liquid return from superhydrophobic condensers. *Int. J. Heat Mass Tran* **2013**, *61*, 409–418. (b) Boreyko, J. B.; Chen, C. H. Self-Propelled Dropwise Condensate on Superhydrophobic Surfaces. *Phys. Rev. Lett.* **2009**, *103* (18), 184501–1–184501–4. (c) Miljkovic, N.; Enright, R.; Nam, Y.; Lopez, K.; Dou, N.; Sack, J.; Wang, E. N. Jumping-Droplet-Enhanced Condensation on Scalable Superhydrophobic Nanostructured Surfaces. *Nano Lett.* **2013**, *13* (1), 179–187. (d) Miljkovic, N.; Wang, E. N. Condensation heat transfer on superhydrophobic surfaces. *MRS Bull.* **2013**, *38* (5), 397–406.

Supporting Information:

# Scalable Graphene Coatings for Enhanced Condensation Heat Transfer

*Daniel J Preston<sup>1</sup>, Daniela L Mafra<sup>2</sup>, Nenad Miljkovic<sup>1,3</sup>, Jing Kong<sup>2</sup>, and Evelyn N Wang<sup>1\*</sup>*

<sup>1</sup>Department of Mechanical Engineering, Massachusetts Institute of Technology, Cambridge, Massachusetts 02139, USA

<sup>2</sup>Department of Electrical Engineering and Computer Science, Massachusetts Institute of Technology, Cambridge, Massachusetts 02139, USA

<sup>3</sup>Department of Mechanical Science and Engineering, University of Illinois, Urbana, Illinois 61801, USA

\*Corresponding author email: [enwang@mit.edu](mailto:enwang@mit.edu)

KEYWORDS: Graphene, condensation, dropwise, heat transfer enhancement, robust, scalable

## S1. ESEM Characterization

The nucleation and initial growth of water droplets on graphene CVD surfaces were studied with an environmental scanning electron microscope (ESEM, Carl Zeiss EVO 50). A bare copper sample which had been annealed at 1000 °C under hydrogen in the CVD chamber but then removed without graphene growth was also examined as a control. The contact angles determined for the graphene CVD surfaces with microgoniometric characterization were confirmed with the ESEM, as shown in Figure S1.

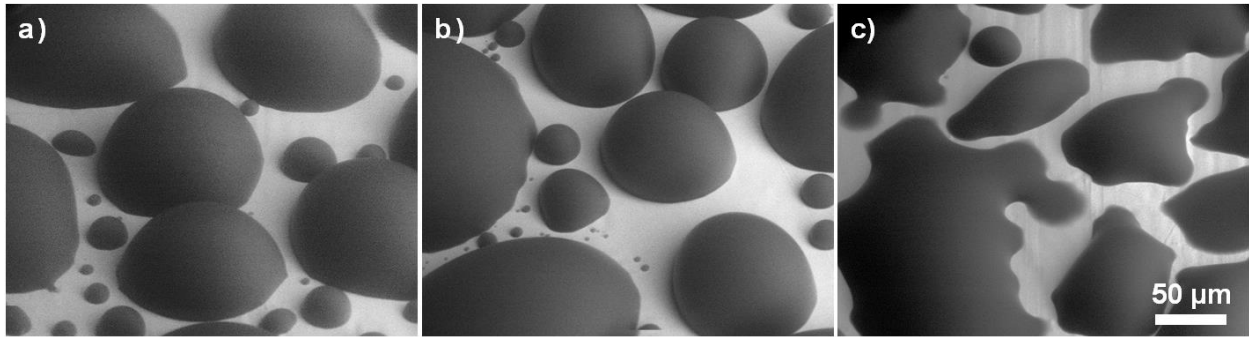


**Figure S1.** ESEM images of condensation on (a) LPCVD graphene on copper, (b) APCVD graphene on copper, and (c) bare copper after annealing in hydrogen. The advancing contact angles of droplets on the graphene-coated copper were approximately 90 degrees, while the advancing contact angle on the bare copper was much lower, resulting in a film as condensation continued.

## S2. Thermal Resistance of Graphene Compared to Substrate

The thermal resistance of a graphene coating is negligible compared to the resistance of the metal surface used to separate the condenser section from the chiller water in a heat exchanger. The thickness for a copper condenser tube wall used in practice is on the order of  $t_{Cu} \approx 0.5$  mm,<sup>1</sup> and copper has a thermal conductivity of  $k_{Cu} \approx 400$  W/m-K. Meanwhile, the thickness for a single-layer graphene coating is approximately  $t_{Gr} \approx 0.5$  nm, and graphene has a thermal conductivity in the transverse direction of  $k_{Gr} \approx 0.1$  W/m-K.<sup>2</sup> Finally, the expected graphene contact resistance for graphene is on the order of  $R_{c,Gr} \approx 10^{-8}$  m<sup>2</sup>-K/W.<sup>3</sup> Taking the ratio of thermal resistance through the copper tube to resistance through the graphene sheet yields:

$$\frac{R_{Cu}}{R_{Gr}} = \frac{t_{Cu}/k_{Cu}}{t_{Gr}/k_{Gr} + R_{c,Gr}} \approx 80 \gg \text{unity} \quad (S1)$$

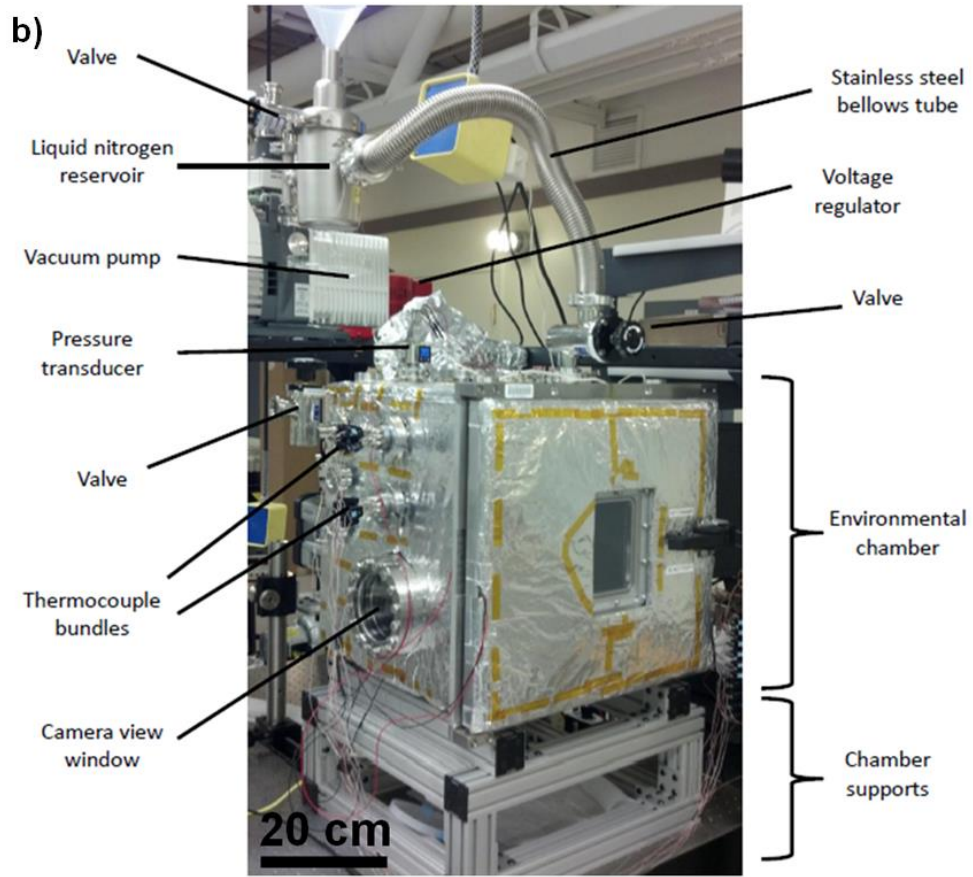
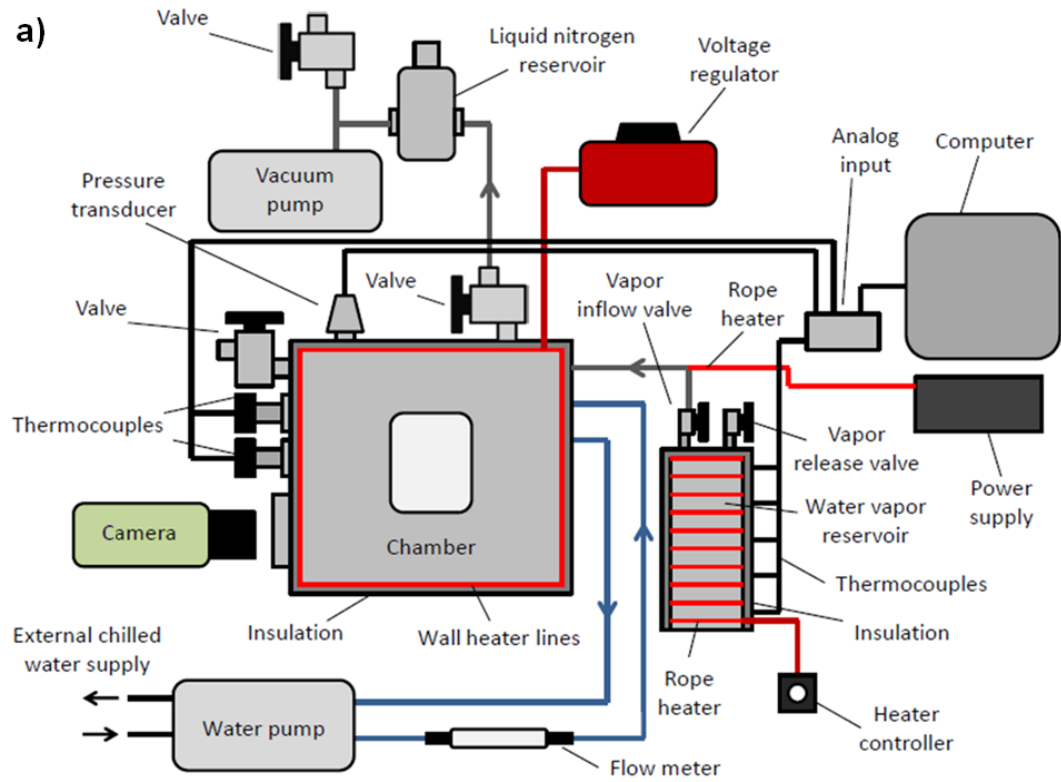
This indicates that the thermal resistance of the metal is much greater than that of the graphene CVD coating, even when considering the thinnest condenser walls widely commercially available and the highest reported values for graphene thermal resistance and contact resistance. For the present study, thicker condenser walls were used which resulted in a thermal resistance ratio of  $R_{Cu}/R_{Gr} > 100$ .

### **S3. Condensation Chamber Setup**

The custom environmental chamber used for this work (Kurt J. Lesker) consists of a stainless steel frame with a door (sealed with a rubber gasket), two viewing windows, and apertures for various components. Resistive heater lines were wrapped around the exterior of the chamber walls to prevent condensation at the inside walls and then insulated on the exterior walls. The output power of the resistive heater lines was controlled by a voltage regulator (Variac). Two insulated stainless steel water flow lines (Swagelok) were fed into the chamber *via* a KF flange port (Kurt J. Lesker) to supply cooling water to the chamber from a large capacity chiller (System III, Neslab).

A secondary stainless steel tube line was fed into the chamber *via* a KF adapter port that served as the flow line for the incoming water vapor supplied from a heated steel water reservoir. The vapor line was wrapped with a rope heater (60 W, Omega) and controlled by a power supply (Agilent). The vapor reservoir was wrapped with another independently-controlled rope heater (120 W, Omega) and insulated to limit heat losses to the environment. The access tubes were welded to the vapor reservoir, each with independently-controlled valves. The first valve (Diaphragm Type, Swagelok), connecting the bottom of the reservoir to the ambient, was used to fill the reservoir with water. The second valve (BK-60, Swagelok), connecting the top of the reservoir to the inside of the chamber, provided a path for vapor inflow. K-type thermocouples were located along the length of the water vapor reservoir to monitor temperature.

A bellows valve (Kurt J. Lesker) was attached to the chamber to serve as a leak port between the ambient and inside of the chamber. In order to monitor temperatures within the chamber, K-type thermocouple bundles were connected through the chamber apertures *via* a thermocouple feed through (Kurt J. Lesker). To provide electrical connections inside the chamber for LED lighting and electric field generation, insulated copper electrical wires were connected through the chamber apertures *via* an electrical feed through (Kurt J. Lesker). A pressure transducer (925 Micro Pirani, MKS) was attached to monitor pressure within the chamber. The thermocouple bundles and the pressure transducer were both electrically connected to an analog input source (RAQ DAQ, National Instruments), which was interfaced to a computer for data recording. A second bellows valve (Kurt J. Lesker) was integrated onto the chamber for the vacuum pump, which brought down the chamber to vacuum conditions prior to vapor filling. A liquid nitrogen cold trap was incorporated along the line from the chamber to the vacuum which served to remove any moisture from the pump-down process and ultimately assist in yielding higher quality vacuum conditions. A tertiary bellows valve (Kurt J. Lesker) was integrated on a T fitting between the vacuum pump and liquid nitrogen reservoir to connect the vacuum line to the ambient to release the vacuum line to ambient conditions once pump down was achieved. In order to visually capture data, a digital SLR camera (Canon EOS 50D) was placed in line with the 5” viewing windows on the chamber. The schematic of the exterior of the environmental setup is depicted in Figure S2a. Images of the front and rear of the experimental setup are shown in Figures S2b and c, respectively.



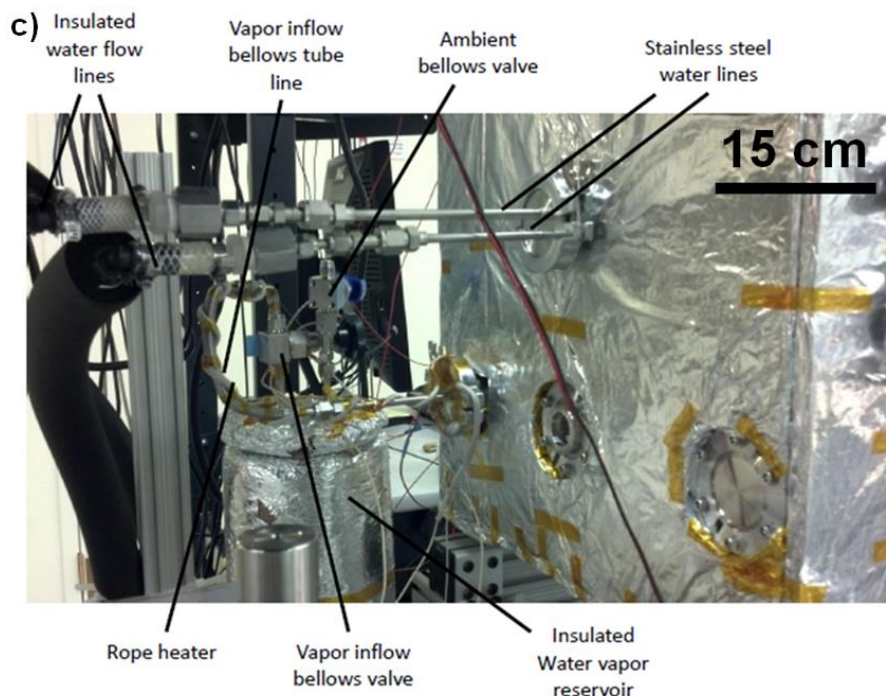


**Figure S2.** (a) Schematic of experimental setup (not to scale). (b) Image of the experimental setup shown from the front (high speed camera and data acquisition system not shown). (c) Image of the experimental setup from the rear of the chamber showing the cooling water inlet and outlet and water vapor reservoir. Reprinted with permission from Reference 4. Copyright 2012 American Chemical Society.<sup>4</sup>

The setup used to run experiments inside the chamber is shown in Figure S3. Stainless steel bellows tube lines (1/4", Swagelok) were connected to the external water flow lines (Figure S2c). T-connection adapters (Swagelok) with bore through Ultra-Torr fittings (Swagelok) were used to adapt K-type thermocouple probes (Omega) at the water inlet and outlet.

The graphene-coated copper tube test sample consisted of a 6.35 mm diameter tube, which was connected *via* a Swagelok compression fitting onto the T-connection. Chilled water flows through the inlet bellows tube, along the inside of the tube sample and through the outlet. Two supports were used to hold the sample and the entire configuration in place. Two separate pieces of insulation were embedded with K-type thermocouple leads and used for wet bulb temperature measurement during experimental runs. A third thermocouple was placed beside the sample to measure the reference temperature inside the chamber.

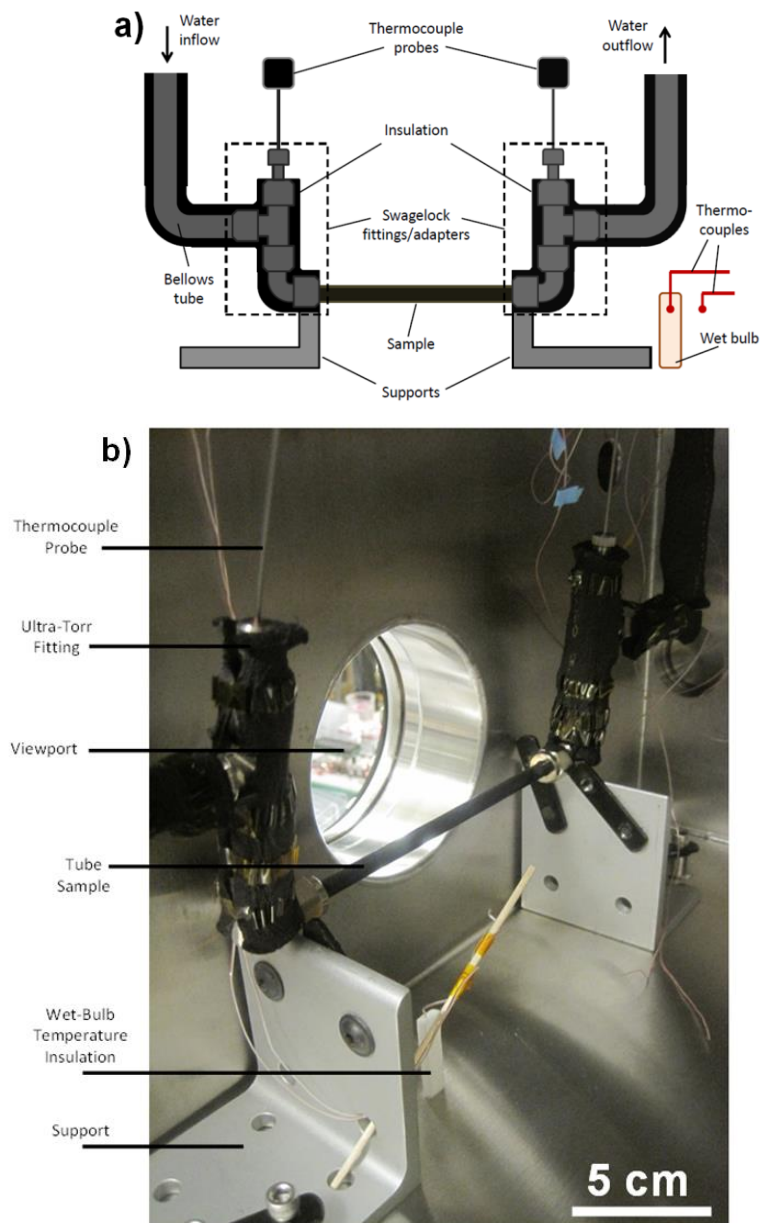


**Figure S3.** (a) Schematic of experimental setup inside the chamber (not to scale). (b) Image of the experimental setup inside the chamber showing a tube in place for testing. Reprinted with permission from Reference 4. Copyright 2012 American Chemical Society.<sup>4</sup>

#### S4. Condensation Procedure

For each experimental trial, a set of strict procedures was followed to ensure consistency throughout the experiments. The first step of the process was to turn on the voltage regulator to

heat up the environmental chamber walls, which prevented condensation on the chamber walls. Simultaneously, the water vapor reservoir was filled with approximately 3.5 liters of DI water (99% full) using a syringe through the vapor release valve. After opening the vapor inflow valve and closing the vapor release valve, the rope heater around the water vapor reservoir was turned on with the heater controller set to maximum output (120 W). Then the rope heater connected to the vapor inflow valve was turned on. The temperature of the water reservoir was monitored with the installed thermocouples; the temperature at the top of the reservoir was higher than that of the middle/bottom of the reservoir due to the water thermal-mass present at the middle/bottom section. Hence, we ensured that the regions of the water reservoir of higher thermal capacity were brought to a sufficiently high temperature for boiling. During the boiling process, aluminum foil was placed on the bottom surface of the inner chamber to collect any of the water leaving the vapor inflow line. Once boiling was achieved and all thermocouples on the reservoir were  $> 95^{\circ}\text{C}$  for at least 10 minutes, the vapor inflow valve was closed. The excess water that spilled inside the chamber during de-gassing of the reservoir was removed.

In order to install the samples onto the rig (Figure S3), the Swagelok female adapters at the ends of the tube samples were connected to the 90 degree male elbow connectors on the rig. Before installing the entire sample setup in the chamber, all adapters/connectors were tightened to ensure that there were no leaks that could affect vacuum performance. The setup was then placed on top of the steel supports and the bellows tubes (for the water inflow/outflow) were connected to the water lines. Then the insulating wet bulb wick was placed near the sample and in contact with the bottom surface of the chamber.

The next step was to begin the vacuum pump-down procedure. Initially, the liquid nitrogen cold trap was filled to about half capacity. The ambient exposed valves connecting the chamber and the vacuum pump were both closed and the valve connected to the liquid nitrogen cold trap was opened. The vacuum pump was then turned on, initiating the pump-down process. The pressure inside the chamber was monitored during the pump-down process. This process took approximately one hour in order to achieve the target vacuum conditions ( $0.5 \text{ Pa} < P < 1 \text{ Pa}$ ). The experimental operating pressure of non-condensable was set to be a maximum of 0.25% of the operating pressure. Non-condensable gas content of above 0.5% (pressure) was shown to

significantly degrade performance during dropwise condensation.<sup>5</sup> In our experiments, extreme care was taken to properly de-gas the vacuum chamber and water vapor reservoir prior to experimental testing. In addition, the chamber leak rate was characterized prior to each run in order to estimate the maximum time available for acquiring high fidelity data with non-condensable content of less than 0.25%.

The setup of the water flow-loop is described as follows: the Neslab water pump reservoir was filled and turned on to a flow rate of 5 L/min ( $0 < \Delta T_{LMTD} < 15$  K). The flow rate was monitored with the flow meter integrated in the inflow water line. In order to bring the chilled water into the flow loop and to the tube sample, the external chilled water lines were opened.

Prior to beginning experiments, the camera was turned on for visual imaging of the sample during condensation. Afterwards, the rope heater around the water reservoir was turned off and the vapor inflow valve was slowly turned open until the operating pressure was reached. Steady state conditions were typically reached after 2 minutes of full operation.

### **S5. Heat Transfer Coefficient and Error Propagation**

An energy balance was applied to the tube sample to determine the overall condensation heat transfer by calculating the change in enthalpy of the chiller water flowing inside the tube:

$$Q = \dot{m}c_p(T_{out} - T_{in}) \quad (S2)$$

where  $Q$  is the overall condensation heat transfer rate,  $\dot{m}$  is the chiller water mass flow rate,  $c_p$  is the chiller water specific heat, and  $T_{in}$  and  $T_{out}$  are the tube inlet and outlet temperatures, respectively. The temperature difference between the chiller water and vapor far from the tube sample was also determined, represented here as the log mean temperature difference (LMTD) to account for the change in temperature of the chiller water along the tube length:

$$\Delta T_{LMTD} = \frac{(T_v - T_{in}) - (T_v - T_{out})}{\ln\left(\frac{T_v - T_{in}}{T_v - T_{out}}\right)} \quad (S3)$$

where  $T_v$  is the temperature of the surrounding vapor far from the tube sample ( $T_v = T_{\text{sat}}(P_v)$ ). From the overall condensation heat transfer and the log mean temperature difference, the overall heat transfer coefficient,  $\bar{U}$ , was determined:

$$\bar{U} = \frac{Q}{A\Delta T_{LMTD}} = \frac{\dot{m}c_p(T_{out} - T_{in})}{A\Delta T_{LMTD}} \quad (\text{S4})$$

where  $A$  is the surface area of the outer tube surface ( $A = 2\pi rL$ , where  $r = 3.175$  mm,  $L = 8.71$  cm). Note that the overall heat transfer coefficient is a function of only the product of experimentally measured parameters raised to powers. Therefore, the error associated with  $\bar{U}$  is calculated as follows:

$$E_{\bar{U}} = \bar{U} \sqrt{\left(\frac{E_{\dot{m}}}{\dot{m}}\right)^2 + \left(\frac{E_{(T_{out}-T_{in})}}{(T_{out} - T_{in})}\right)^2 + \left(\frac{-E_A}{A}\right)^2 + \left(\frac{-E_{\Delta T_{LMTD}}}{\Delta T_{LMTD}}\right)^2} \quad (\text{S5})$$

The condensation heat transfer coefficient can be extracted from  $\bar{U}$  by considering a series of thermal resistances that sum to  $\bar{U}$  and isolating the resistance associated with condensation:

$$\frac{1}{\bar{U}A} = \frac{1}{h_i A_i} + R_t + \frac{1}{h_c A} \quad (\text{S6})$$

Rearranging to evolve explicitly for  $h_c$ :

$$h_c = \left(\frac{1}{\bar{U}} - \frac{A}{h_i A_i} - R_t A\right)^{-1} \quad (\text{S7})$$

where  $A_i$  is the surface area on the inner surface of the tube ( $A_i = 2\pi r_i L$ ),  $R_t$  is the thermal resistance of the tube ( $R_t = \ln(r/r_i)/(2\pi k_t)$ ,  $k_t$  is the tube material thermal conductivity), and the internal heat transfer coefficient,  $h_i$ , is determined from the Gnielinski correlation for pipe flow:

$$h_i = \left(\frac{k_i}{2r_i}\right) \frac{(f/8)(Re - 1000)Pr}{1 + 12.7(f/8)^{1/2}(Pr^{2/3} - 1)} \quad (\text{S8})$$

$$f = (0.790 \ln Re - 1.64)^{-2} \quad (\text{S9})$$

$$Re = \frac{\rho v(2r_i)}{\mu} \quad (\text{S10})$$

where  $f$  is the friction factor,  $Re$  is the Reynolds number,  $Pr$  is the Prandtl number,  $\rho$  is the chiller water density,  $k_i$  is the chiller water thermal conductivity, and  $\mu$  is the chiller water dynamic viscosity. Solving for  $h_i$  and substituting into the above Equation S7 allows for determination of  $h_c$ . As  $h_c$  is not a simple function of a product of powers, the error is determined as a function of the first partial derivatives of  $h_c$  with respect to its components.

$$E_{h_c} = h_c \sqrt{\left(\frac{\partial h_c}{\partial h_i} E_{h,i}\right)^2 + \left(\frac{\partial h_c}{\partial \bar{U}} \frac{E_{\bar{U}}}{\bar{U}}\right)^2} \quad (\text{S11})$$

$$\frac{\partial h_c}{\partial h_i} = \frac{-(A/A_i)\bar{U}^2}{(h_i - (A/A_i)\bar{U} - R_t A \bar{U} h_i)^2} \quad (\text{S12})$$

$$\frac{\partial h_c}{\partial \bar{U}} = \frac{h_i^2}{(h_i - (A/A_i)\bar{U} - R_t A \bar{U} h_i)^2} \quad (\text{S13})$$

The error in  $\bar{U}$  was determined in Equation S5 and the error in  $h_i$  was estimated as 10% associated with the Gnielinski correlation.<sup>6</sup> Table S1 below summarizes the uncertainty associated with each experimental measurement.

**Table S1. Uncertainties corresponding to experimental measurements.**

Experimental Measurement	Uncertainty
Chiller water temperature difference ( $T_{out} - T_{in}$ )	0.05K
Saturated vapor pressure ( $P_v$ )	1%
Saturated vapor temperature ( $T_v$ )	$T_{sat}(1.01(P_v)) - T_{sat}(P_v)$
Chiller water mass flow rate ( $\dot{m}$ )	2%
Sample surface area ( $A$ )	2%
Gnielinski correlation heat transfer coefficient ( $h_i$ )	10%

## S6. Modeling of Heat Transfer Coefficient

To model dropwise condensation,  $h_{c,d}$  was obtained by incorporating the individual droplet heat transfer with droplet size distribution:<sup>7</sup>

$$h_{c,d} = \frac{q''}{\Delta T} = \frac{1}{\Delta T} \left( \int_{R^*}^{R_c} q(R)n(R)dR + \int_{R_c}^{\hat{R}} q(R)N(R)dR \right) \quad (S14)$$

$$q(R) = \frac{\pi R^2 \left( \Delta T - \frac{2T_{sat}\sigma}{Rh_{fg}\rho_w} \right)}{\frac{1}{2h_{int}(1 - \cos \theta)} + \frac{R\theta}{4k_w \sin \theta} + \frac{1}{k_{HC} \sin^2 \theta} \left( \frac{k_P \varphi}{\delta_{HC} k_P + h k_{HC}} + \frac{k_W(1 - \varphi)}{\delta_{HC} k_W + h k_{HC}} \right)^{-1}} \quad (S15)$$

where  $q''$  is the steady state dropwise condensation heat transfer rate per unit area of the condensing surface,  $\Delta T$  is the temperature difference between the saturated vapor and sample outer surface ( $\Delta T = (T_{sat}(P) - T_s)$ ),  $R^*$  is the critical radius for heterogeneous nucleation ( $R^* = r_c$ ),<sup>8</sup>  $R_c$  is the droplet coalescence radius,  $q(R)$  is the individual droplet heat transfer (Equation S15),  $n(R)$  is the non-interacting droplet size distribution,<sup>7</sup>  $N(R)$  is the coalescence dominated droplet size distribution,<sup>7, 9</sup>  $R$  is the droplet radius,  $\sigma$  is the condensate surface tension,  $h_{fg}$  is the latent heat of phase change,  $\rho_w$  is the condensate density (liquid water),  $\theta$  is the droplet contact angle,  $h_{int}$  is the interfacial heat transfer coefficient,<sup>10</sup>  $k_w$  is the condensate thermal conductivity,  $k_{HC}$  is the hydrophobic coating thermal conductivity,  $\varphi$  is the structured surface solid fraction (equal to one for the flat surfaces considered here),  $h$  is the structured surface height (equal to zero for flat surfaces), and  $\delta_{HC}$  is the hydrophobic coating thickness ( $\approx 1$  nm).<sup>8</sup> The first integral in Equation S14 represents the heat flux component from droplets smaller than the coalescence length scale

( $R < R_e$ ), where direct growth by vapor accommodation at the liquid-vapor interface dominates and neighboring droplet coalescence is absent. The second integral represents the component of the heat flux from droplets growing mainly by coalescence with other droplets ( $R > R_e$ ). These two components contribute to the total surface heat transfer per unit area ( $q''$ ). For the graphene-coated surfaces, the model results were obtained using experimentally determined droplet departure radii  $\hat{R}$  ( $\hat{R}_{LPCVD} = 2.4$  mm,  $\hat{R}_{APCVD} = 2.8$  mm) and contact angles, and assuming an effective nucleation density  $N$  from previous ESEM studies of condensation.<sup>11</sup>

To model filmwise condensation on the smooth Cu tubes, the Nusselt model was used:<sup>6,10</sup>

$$h_{c,f} = 0.729 \left( \frac{g \rho_w (\rho_w - \rho_v) k_w^3 h'_{fg}}{\mu_w (2r) \Delta T} \right)^{1/4} \quad (\text{S16})$$

$$h'_{fg} = h_{fg} + 0.68 c_{p,l} \Delta T \quad (\text{S17})$$

where  $g$  is the gravitational acceleration ( $g = 9.81$  m/s<sup>2</sup>),  $\rho_v$  is the water vapor density,  $\mu_w$  is the condensate dynamic viscosity,  $h'_{fg}$  is the modified latent heat of vaporization accounting for the change in specific heat of the condensate, and  $c_{p,l}$  is the condensate specific heat.<sup>6,10</sup>

An example of the dropwise and filmwise heat transfer coefficients as a function of condenser subcooling yielded from the above models is plotted in Figure S4 under typical experimental conditions. The dropwise condensation heat transfer coefficient decreases at low subcooling because the interfacial heat transfer coefficient becomes a major resistance to heat transfer.<sup>5b, 12</sup> Meanwhile, the filmwise condensation heat transfer coefficient increases at low subcooling as the film becomes thinner at low heat fluxes<sup>13</sup> (note that, although the heat transfer coefficient is increasing, the heat flux is decreasing). Furthermore, the Nusselt theory used for filmwise condensation does not consider the interfacial heat transfer coefficient, which would decrease the heat transfer coefficient at low subcooling in competition with the increase due to the thinner film. This results in the dropwise and filmwise heat transfer coefficients approaching each other as subcooling decreases.

In the present study, the condenser subcooling ranged from  $\approx 1.5$ -6 K, with the experimentally measured heat transfer coefficients shown in Figure 4b obtained at condenser subcooling ranging from 3.5-5 K while varying vapor pressure (the horizontal axis) and maintaining the supersaturation,  $S = P_{\text{vapor}}/P_{\text{sat}}(T_{\text{wall}})$ , constant over the range of data. The experimentally determined heat transfer coefficient enhancement of 4x for dropwise condensation on graphene-coated tubes compared to filmwise condensation is in excellent agreement with the model shown in Figure S4 in the 3.5-5 K subcooling range where the experimental measurements were taken. Note that, at higher subcooling over  $\approx 10$  K, the typically reported 5-7x heat transfer coefficient enhancement<sup>5b</sup> for dropwise compared to filmwise condensation would be realized.

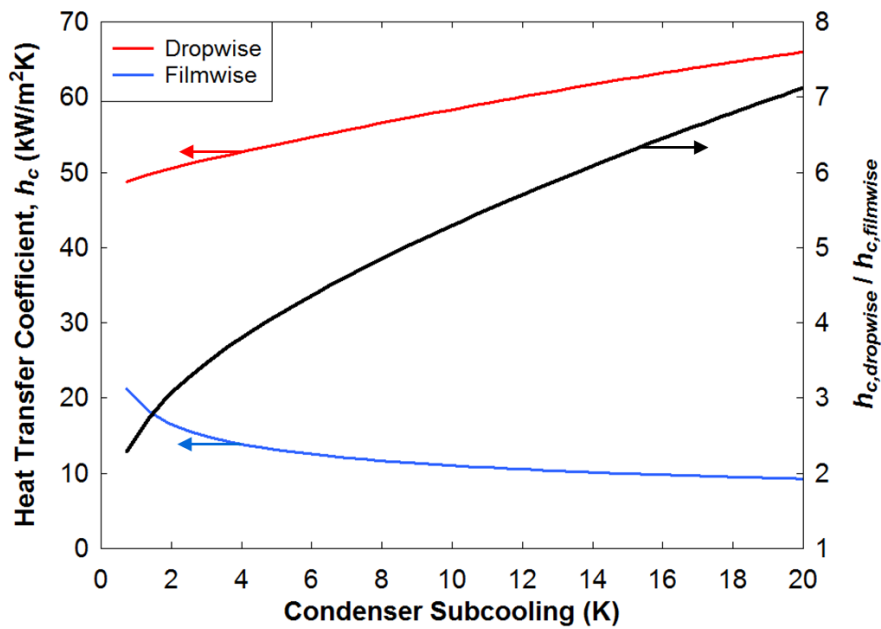


**Figure S4.** Plot of model results for filmwise and dropwise condensation heat transfer coefficient as a function of condenser subcooling, keeping the condenser temperature constant at 15.5 °C ( $P_{\text{sat}} = 1780$  Pa) and varying the surrounding saturated water vapor temperature from 16 to 35.5 °C ( $P_{\text{sat}} = 1840$  to 5860 Pa). The secondary (right) vertical axis is the ratio of dropwise to filmwise condensation heat transfer coefficients.

## S7. Robustness Characterization Setup and Operation

The robustness of the graphene coatings was characterized in a controlled positive-pressure continuous condensation chamber, shown in Figure S5. The robustness characterization setup is

a thermosiphon with the samples located at the condenser section, where they are observed periodically to monitor degradation. A 1/4" thick borosilicate window was fit on a stainless steel chamber, and the 3/4"x3/4" square copper samples being tested are secured to the interior surface of the back wall of the chamber. The exterior of the back wall was in thermal contact with a Peltier cold stage with 100W cooling capacity. A separate reservoir filled with degassed, deionized water was located 0.5 m below the chamber. Heaters on the exterior of the reservoir raised the water temperature to above 100 °C, and the resulting vapor then traveled through a supply line up to the chamber, where it condensed on the chamber walls and also escaped through a check valve rated for 0.1 psig due to the overpressure from boiling in the reservoir. The condensed vapor transported to the bottom of the chamber, where it collected until it flowed under the influence of gravity back to the reservoir.

To eliminate noncondensable gases (NCGs) from the system before operation, the water in the reservoir was boiled vigorously while the chamber was heated by the Peltier stage and also externally by a hot air gun to prevent condensation on the chamber walls and the subsequent trapping on NCGs in a diffusion boundary layer. This purge step was carried out until the system contains nearly pure saturated water/vapor. After the purge process, the system was constantly maintained at positive pressure to prevent NCGs from reentering. The system was overpressurized by boiling slightly more water than is condensed, resulting in water leaving the check valve and signifying that the system is at > 0.1 psig. Once the system had reached this steady operating condition, the Peltier stage was switched to cooling mode, where in the present study the samples were cooled to a surface temperature of  $95\pm 1$  °C and exposed to a continuous supply of 100 °C steam, as determined by thermocouples mounted in the system. The durability of the graphene-coated samples is shown to be comparable to the highest-quality polymer CVD coatings.<sup>14</sup>

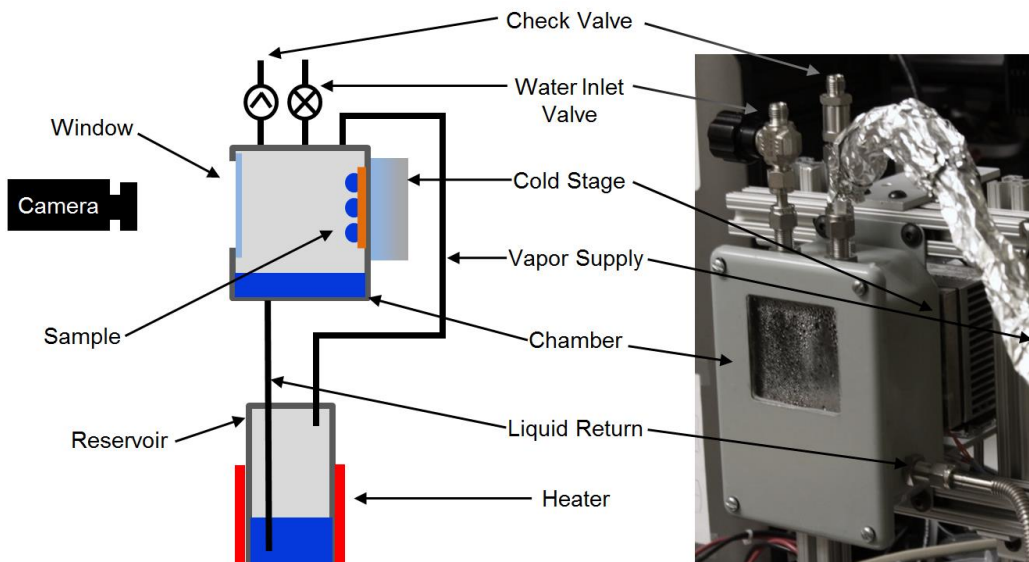


**Figure S5.** Schematic of experimental robustness characterization setup, which is comprised of a thermosiphon operating between a hot reservoir and a cold condenser section where the samples were imaged periodically to monitor degradation.

### S8. Comparison with Previous Work on Graphene Robustness

The LPCVD and APCVD graphene coated samples both sustained dropwise condensation for over two weeks with no signs of degradation when the experiments were discontinued. This result agrees with past work that demonstrates experimentally that destruction of a graphene coating does not occur by oxidation below 400 °C<sup>15</sup> and that graphene prevents oxidation of copper surfaces and is an excellent passivation layer.<sup>16</sup> However, subsequent literature states that this passivation is only valid for short times (hours), after which the coatings can fail due to oxidation of copper at graphene grain boundaries.<sup>17</sup> These experiments were conducted at 185-250 °C, above our condenser surface temperature of  $\approx 95$  °C; accordingly, a thermally activated oxidation process would be expected to take longer for our lower-temperature test. Regardless, over two weeks, we did not observe oxidation or degradation in our experiments, which agrees with the studies which show that oxidation is mitigated.

### S9. Graphene Transfer to Transparent Substrate

The graphene was transferred to a transparent substrate by the electrochemical delamination transfer process.<sup>18</sup> This process removes the need for Cu etchant to detach the graphene from the

Cu, which consequently avoids the large quantity of etchant waste from the relatively thick Cu sample on which the graphene was grown. After the graphene growth, poly(methyl methacrylate) (PMMA) (950 PMMA A9, Micro Chem, mixed with anisole (99%, Alfa Aesar) 1:1 by volume) was spun on one side of the graphene/copper substrate. After baking at  $\sim 75$  °C for 5 minutes, the substrate was cathodically polarized at  $-5$  V, and an aqueous solution of NaOH (10 mM) was employed as an electrolyte in the electrochemical process. Hydrogen bubbles emerged at the graphene/Cu interfaces due to the reduction of water and detached the graphene film from the Cu foil. The graphene/PMMA was then placed on top of the transparent substrate. The PMMA layer was removed by annealing the substrate at 500 °C in a hydrogen (700 sccm) and argon (400 sccm) mixture for two hours.

### S10. Graphene Coating Cost Estimate

The cost of the graphene coatings is estimated here for the lab-scale production procedure. The costs used are conservative; moving to industrial scale fabrication, process optimization, and using less conservative cost estimates is expected to reduce the price by several orders of magnitude. The gas prices at the lab scale are (for 300 ft<sup>3</sup> per cylinder, prices obtained from airgas.com on 12 February 2015):

Gas	Cylinder Price (\$)	Volumetric Gas Price (\$/m <sup>3</sup> )
Argon (Ultra High Purity)	81.08	9.55
Hydrogen (Ultra High Purity)	140.24	16.52
Methane(Ultra High Purity)	323.11	38.06

Prescribing the gas consumption according to the CVD process detailed in the manuscript, and assuming that 10 tube condenser samples of the geometry used in the present study are being coated simultaneously for a total external surface area of 0.0174 m<sup>2</sup>, the overall prices for gases for the CVD process are summarized as:

<b>LPCVD</b>		<b>APCVD</b>	
Flow phase 1 H <sub>2</sub>	10 sccm	Flow phase 1 Ar	500 sccm
Time phase 1	30 min	Time phase 1	30 min
Flow phase 2 H <sub>2</sub>	70 sccm	Flow phase 2 Ar	500 sccm
Flow phase 2 CH <sub>4</sub>	4 sccm	Flow phase 2 CH <sub>4</sub>	3 sccm
Time phase 2	30 min	Time phase 2	30 min

Flow phase 3 H <sub>2</sub>	10 sccm	Flow phase 3 Ar	500 sccm
Time phase 3	120 min	Time phase 3	120 min
H <sub>2</sub> total consumed	3600 cm <sup>3</sup>	H <sub>2</sub> total consumed	90000 cm <sup>3</sup>
CH <sub>4</sub> total consumed	120 cm <sup>3</sup>	CH <sub>4</sub> total consumed	90 cm <sup>3</sup>
H <sub>2</sub> total consumed	0.0036 m <sup>3</sup>	H <sub>2</sub> total consumed	0.09 m <sup>3</sup>
CH <sub>4</sub> total consumed	0.00012 m <sup>3</sup>	CH <sub>4</sub> total consumed	0.00009 m <sup>3</sup>
Gas total price	0.064 \$	Gas total price	0.863 \$
Gas price per area	3.69 \$/m <sup>2</sup>	Gas price per area	49.66 \$/m <sup>2</sup>

Taking the power required to heat the furnace as the maximum furnace power of 800W for the 1-inch diameter tube furnace (Thermo Scientific Lindberg/Blue M Tube Furnace C2) over the operating period of 1.5hr including a 0.5-hour ramp period yields the cost of electricity:

Furnace power	0.8 kW
Heating time	1.5 hr
Energy consumed	1.2 kWh
Price of electrical energy	0.12 \$/kWh
Total price of electricity	0.144 \$
Electricity price per area	8.29 \$/m <sup>2</sup>

Therefore, summing the price per area of electricity and gas consumption, the lab-scale non-optimized costs for CVD graphene coatings are \$11.98/m<sup>2</sup> for LPCVD and \$57.95/m<sup>2</sup> for APCVD.

### Supplementary Material References

- Trane Heat Exchanger Options. <http://www.trane.com> (accessed October 2014);
  - Gamza, J. Optimizing Condenser Tube Life with Nondestructive Testing. <http://www.concosystems.com> (accessed October 2014);
  - HTS Fluid Heat Transfer: RAE Coils - Condenser Coils. <http://www.htseng.com/relinfostore/> (accessed October 2014).
- Balandin, A. A., Thermal properties of graphene and nanostructured carbon materials. *Nat Mater* **2011**, *10* (8), 569-581;
  - Wei, Z. Y.; Ni, Z. H.; Bi, K. D.; Chen, M. H.; Chen, Y. F., Interfacial thermal resistance in multilayer graphene structures. *Phys Lett A* **2011**, *375* (8), 1195-1199;
  - Delhaes, P., *Graphite and precursors*. Gordon & Breach: Australia, 2001; p xiv, 297 p.

3. Shahil, K. M. F.; Balandin, A. A., Thermal properties of graphene and multilayer graphene: Applications in thermal interface materials. *Solid State Commun* **2012**, *152* (15), 1331-1340.
4. Miljkovic, N.; Enright, R.; Nam, Y.; Lopez, K.; Dou, N.; Sack, J.; Wang, E. N., Jumping-Droplet-Enhanced Condensation on Scalable Superhydrophobic Nanostructured Surfaces. *Nano Lett* **2013**, *13* (1), 179-187.
5. (a) Ma, X. H.; Zhou, X. D.; Lan, Z.; Li, Y. M.; Zhang, Y., Condensation Heat Transfer Enhancement in the Presence of Non-Condensable Gas Using the Interfacial Effect of Dropwise Condensation. *Int J Heat Mass Tran* **2008**, *51* (7-8), 1728-1737; (b) Rose, J. W., Dropwise condensation theory and experiment: a review. *P I Mech Eng a-J Pow* **2002**, *216* (A2), 115-128.
6. Incropera, F. P., *Introduction to heat transfer*. 5th ed.; Wiley: Hoboken, N.J., 2007; p xxv, 901 p.
7. Miljkovic, N.; Enright, R.; Wang, E. N., Modeling and Optimization of Superhydrophobic Condensation. *Journal of Heat Transfer* **2013**, *135* (11), 111004-111004.
8. Kaschiev, D., *Nucleation: Basic Theory With Applications*. Butterworth Heinemann: Oxford, 2000.
9. Rose, J. W.; Glicksman, L. R., Dropwise condensation - the distribution of drop sizes. *Int J Heat Mass Tran* **1973**, *16*, 411-425.
10. Carey, V. P., *Liquid-vapor phase-change phenomena : an introduction to the thermophysics of vaporization and condensation processes in heat transfer equipment*. 2nd ed.; Taylor and Francis: New York, 2008; p xxii, 742 p.
11. Enright, R.; Dou, N.; Miljkovic, N.; Nam, Y.; Wang, E. N., Condensation on Superhydrophobic Copper Oxide Nanostructures. *Proceedings of the Asme Micro/Nanoscale Heat and Mass Transfer International Conference, 2012* **2012**, 419-425.
12. (a) Wilmshurst, R.; Rose, J. W., Dropwise Condensation—Further Heat Transfer Measurements. In *Fourth International Heat Transfer Conference*, Elsevier: Paris-Versailles, France, 1970; Vol. 6; (b) Enright, R.; Miljkovic, N.; Alvarado, J. L.; Kim, K. J.; Rose, J. W., Dropwise Condensation on Micro- and Nanostructured Surfaces. *Nanoscale and Microscale Thermophysical Engineering* **2014**.
13. Nusselt, W., The surface condensation of water vapour. *Z Ver Dtsch Ing* **1916**, *60*, 541-546.

14. Paxson, A. T.; Yague, J. L.; Gleason, K. K.; Varanasi, K. K., Stable Dropwise Condensation for Enhancing Heat Transfer via the Initiated Chemical Vapor Deposition (iCVD) of Grafted Polymer Films. *Adv Mater* **2013**.
15. Liu, L.; Ryu, S. M.; Tomasik, M. R.; Stolyarova, E.; Jung, N.; Hybertsen, M. S.; Steigerwald, M. L.; Brus, L. E.; Flynn, G. W., Graphene oxidation: Thickness-dependent etching and strong chemical doping. *Nano Lett* **2008**, *8* (7), 1965-1970.
16. Chen, S. S.; Brown, L.; Levendorf, M.; Cai, W. W.; Ju, S. Y.; Edgeworth, J.; Li, X. S.; Magnuson, C. W.; Velamakanni, A.; Piner, R. D.; Kang, J. Y.; Park, J.; Ruoff, R. S., Oxidation Resistance of Graphene-Coated Cu and Cu/Ni Alloy. *Acs Nano* **2011**, *5* (2), 1321-1327.
17. Schriver, M.; Regan, W.; Gannett, W. J.; Zaniewski, A. M.; Crommie, M. F.; Zettl, A., Graphene as a Long-Term Metal Oxidation Barrier: Worse Than Nothing. *Acs Nano* **2013**, *7* (7), 5763-5768.
18. (a) Gao, L. B.; Ren, W. C.; Xu, H. L.; Jin, L.; Wang, Z. X.; Ma, T.; Ma, L. P.; Zhang, Z. Y.; Fu, Q.; Peng, L. M.; Bao, X. H.; Cheng, H. M., Repeated growth and bubbling transfer of graphene with millimetre-size single-crystal grains using platinum. *Nat Commun* **2012**, *3*; (b) Wang, Y.; Zheng, Y.; Xu, X. F.; Dubuisson, E.; Bao, Q. L.; Lu, J.; Loh, K. P., Electrochemical Delamination of CVD-Grown Graphene Film: Toward the Recyclable Use of Copper Catalyst. *Acs Nano* **2011**, *5* (12), 9927-9933.